The Effect of Calibration Factors and Recovery Coefficients on ^{177}Lu SPECT Activity Quantification Accuracy: A Monte Carlo Study

Keamogetswe Ramonaheng (BoomK@ufs.ac.za)
University of the Free State Faculty of Health Sciences https://orcid.org/0000-0002-5837-9303
Johan A van Staden
University of the Free State Faculty of Health Sciences
Hanlie du Raan
University of the Free State Faculty of Health Sciences

Original research

Keywords: 177Lu, Quantification, Monte Carlo, SIMIND, Calibration factor, Recovery coefficients

Posted Date: October 12th, 2020

DOI: https://doi.org/10.21203/rs.3.rs-88650/v1

Version of Record: A version of this preprint was published at EJNMMI Physics on March 18th, 2021. See the published version at https://doi.org/10.1186/s40658-021-00365-8.

Abstract

Background: Different gamma camera calibration factor (CF) geometries have been proposed to convert SPECT data into units of activity concentration. However, no consensus has been reached on a standardized geometry. The CF is dependent on the selected geometry and affected by partial volume effects. This study investigated the effect of two CF geometries and their corresponding recovery coefficients (RCs) on the quantification accuracy of ^{177}Lu SPECT images using Monte Carlo simulations.

Methods: The CF geometries investigated were (i) a radioactive-sphere surrounded by non-radioactive water (sphere-CF) and (ii) a cylindrical phantom uniformly filled with radioactive water, (cylinder-CF). Recovery coefficients were obtained using the sphere-CF and cylinder-CF, yielding the sphere-RC and cylinder-RC values, respectively, for partial volume correction (PVC). The quantification accuracy was evaluated using four different sized spheres (15.6 ml – 65.4 ml) and a kidney model with known activity concentrations inside a cylindrical, torso and patient phantom. Images were reconstructed with the OS-EM algorithm incorporating attenuation, scatter and detector-response corrections. Segmentation was performed using the physical size and a small cylindrical volume inside the cylinder for the sphere-CF and cylinder-CF, respectively.

Results: The sphere quantification error (without PVC) was better for the sphere-CF (≤ -5.54%) compared to the cylinder-CF (≤ -20.90%), attributed to the similar geometry of the quantified and CF spheres. Partial volume correction yielded comparable results for the sphere-CF (≤ 3.47%) and cylinder-CF (≤ 3.53%). The accuracy of the kidney quantification was poorer (≤ 22.34%) for the sphere-CF without PVC compared to the cylinder-CF (≤ 2.44%). With PVC, the kidney quantification results improved and compared well for the sphere-CF (≤ 3.50%) and the cylinder-CF (≤ 3.45%).

Conclusion: The study demonstrated that upon careful selection of CF-RC combinations, comparable quantification errors (≤ 3.53%) were obtained between the sphere-CF and cylinder-CF, when all corrections were applied.

1. Background

Lutetium-177 (^{177}Lu) has become widely used for targeted radionuclide therapy in nuclear medicine [1]. This is owing to its favorable decay characteristics as both a therapeutic as well as an imaging agent [2]. In addition, it is produced with high specific activity and exhibits reliable labelling of peptides used for tumor targeting [3, 4]. ^{177}Lu has gained favor in the clinical application of peptide receptor radionuclide therapy (PRRT) with ^{177}Lu-DOTATATE for the treatment of patients with late-stage metastatic neuroendocrine tumors [5–9]. The kidneys have been identified as the dose-limiting organs for ^{177}Lu-DOTATATE PRRT [10]. A significant correlation was found between the tumor-absorbed dose and tumor reduction [11]. Therefore, dosimetry should be extended to include both the kidneys and tumor sites to provide a satisfactory understanding of PRRT treatment. There is a large variation in kidney and tumor

response among patients following PRRT [12, 13]. This would facilitate the application of accurate patient-specific dosimetry for PRRT treatment planning, as is the norm in external beam radiotherapy.

Accurate dosimetry is strongly dependent on the accuracy with which activity quantification can be achieved. The imaging and quantification process is not ideal and therefore has been investigated and refined for many years [14–17]. There are factors inherent in the imaging process that degrade the images from an ideal representation of the imaged object. These factors include photon attenuation and scattering, collimator blurring, partial volume effects (PVEs), and the reconstruction algorithms [18]. SPECT/CT images have been included in many dosimetry protocols for ^{177}Lu activity quantification, and this is owing to their superior quantitative accuracy in comparison to planar images [19, 20]. However, the effects of the above-mentioned degrading factors complicate SPECT imaging. Therefore, attempts to compensate for these factors have to be made to improve the accuracy of the quantified activity.

The 3D ordered subset expectation maximization (OS-EM) iterative reconstruction algorithm [21] can include modelling of the physical characteristics of the imaging process. These may include compensation for photon attenuation, photon scatter and collimator detector response (CDR). This algorithm results in reconstructed images with better image quality, improved quantitative accuracy, and which are less prone to artefacts in comparison to the analytical methods such as filtered back projection [22, 23, 24]. The 3D OS-EM reconstruction algorithm has become a standard algorithm with most clinical SPECT processing units; it is highly recommended and commonly used to obtain improved quantitative SPECT data [25]. An important consideration when using the above-mentioned 3D OS-EM reconstruction algorithm is the optimum number of updates which is defined as the product of the number of subsets and iterations. The criteria for the optimum number of 3D OS-EM updates has been accepted as the convergence where 90% of the activity has been recovered [26]. Complex reconstruction algorithms incorporating more corrections require a larger number of iterations to reach convergence, and larger objects have been shown to converge faster than smaller objects [27]. It is recommended that phantom or Monte Carlo (MC) simulation studies be used to investigate the optimum number of 3D OS-EM updates needed to provide adequate convergence for accurate activity quantification [16]. The optimization is unique to a specific SPECT system and associated reconstruction algorithm as well as the imaging geometry.

The X-ray CT in hybrid SPECT/CT systems has provided an automated way to compensate for object attenuation. The availability of the co-registered SPECT and CT data has made routine attenuation compensation practical and easy to implement. Multiple window scatter compensation methods such as the Dual Energy Window (DEW) and the Triple Energy Window (TEW) methods are available with most gamma camera vendors, and these methods can be used to apply scatter correction during or post-reconstruction. However, model-based scatter correction methods, such as effective source scatter estimation (ESSE), model the scatter function more accurately and thus better resemble the true scatter distribution [28]. The ESSE method uses MC simulations to pre-calculate a set of scatter kernels to estimate the degrading scatter effect from a slab of material (mimicking tissue) for a point source at a set of distances from the collimator face. The MC simulation methods are also used to model the

geometric response, septal penetration and septal scatter response functions of the gamma camera from a point source in air. For SPECT imaging purposes, these response functions are incorporated during reconstruction to improve spatial resolution. Volume of interest (VOI) definition for object delineation is also an important consideration for quantification of SPECT images, and no standardized method has yet been identified. CT data has been used in a number of clinical and phantom studies for object delineation [17, 29]. The impact of errors due to misdefinition (variability in organ delineation) and misregistration (between emission and CT data) on SPECT and planar quantification accuracy has been investigated [30]. The VOI definition is affected by PVEs, which has a larger impact on smaller objects with size smaller than three times the system spatial resolution (3 × FWHM) [31]. The PVE is related to the gamma cameras limited spatial resolution and can be reduced by including a CDR correction during the iterative reconstruction process. A consequence of the PVE is that the photon originating from a point will contribute not only to a single voxel but also to neighboring voxels. This is known as spill-out of counts and is widely seen in tumor imaging and reported to result in underestimation of the quantified activity distribution [32]. Conversely, spill-in of counts from surrounding radioactive objects is also observed resulting in an overestimation of the quantified activity. If this spill-in and spill-out of counts at the edges of objects is not compensated for, it will result in biased quantification results [18]. Recovery coefficients (RCs) for partial volume correction (PVC) can easily be implemented in phantom studies where true activity and object size can be measured [33]. CT-based RCs have been successfully used for PVC in ^{177}Lu SPECT activity quantification in a torso phantom [15] and extended to 3D printed kidney phantoms [29]. Another important consideration of PVE is image sampling. Due to the limited voxel size, a combination of objects having different activity concentrations may contribute to a specific voxel count. Thus, a small shift in the delineated region can result in a significant variation in counts. The extent of the variation can be limited by using smaller voxel sizes [34].

SPECT was traditionally regarded as a non-quantitative imaging modality, unlike its counterpart PET. In both modalities, advances in hybrid systems include automation of compensation methods for photon attenuation, scatter and limited spatial resolution in a unified manner using iterative reconstruction algorithms. In general, SPECT images are obtained in units of image counts, unlike PET reconstructed images which have units of tissue radioactive concentration (kBq.cm^{-3}). Thus, a calibration factor (CF) has to be applied to obtain SPECT reconstructed images in units of radioactive concentration. It is only recently, with modern SPECT/CT systems, that reconstructed SPECT images are routinely provided in units of radioactive concentration. An example of such a SPECT/CT system is the Siemens Symbia Intevo™ scanner (Siemens Healthineers, Germany), which incorporates a point source traceable to a secondary standard laboratory for calibration purposes and conversion of the reconstructed SPECT images to activity concentration.

The system sensitivity, as defined by the National Electrical Manufacturers Association, is conventionally used as a CF in SPECT images to convert the quantified counts into units of activity [35–38]. It is generally accepted that the CF, with a source geometry that incorporates photon attenuation and scatter properties in the acquisition reduces the effects of imperfect scatter and attenuation corrections [26].

Different geometries have been reported for obtaining CFs for the purpose of ^{177}Lu SPECT quantitative imaging [39]. The authors investigated four geometries to obtain CFs which included; a point source in air, a sphere in air, a sphere in non-radioactive water and a 20 cm diameter cylinder uniformly filled with $^{177}LuCl_3$. The point source in air and the sphere in water yielded the poorest and best results respectively for the activity quantification in an anthropomorphic torso phantom. The sphere in a non-radioactive background was reported as suitable for activity quantification of ^{177}Lu SPECT data using the 208 keV photopeak. Superior quantification accuracy has been found for SPECT imaging with a CF obtained using a sphere in a radioactive background (sphere-to-background ratio of 6:1) compared to that obtained using a cylindrical phantom uniformly filled with ^{131}I [27]. The authors also reported the sphere CF yielded more stable results compared to a point source in air which is highly sensitive to the selected VOI size. Due to down-scatter and septal penetration from high energy photons into the photopeak window for isotopes such as ^{131}I and ^{188}Re, Zhao et al. suggested that a CF obtained from a planar point source must include scatter correction for these isotopes, and to a lesser extent for the ^{177}Lu 208 keV photopeak [40]. In addition, the study showed that CFs obtained using spheres in a non-radioactive background may underestimate the CF by 10% attributed to the scatter approximation by the TEW method and accentuated further by the attenuation correction during reconstruction.

The disparities between ^{177}Lu SPECT activity quantification accuracy reported by different authors for various phantoms, as well as their data acquisition and processing protocols, has been summarized in the MIRD pamphlet 26 [16]. The MIRD pamphlet 26 also documents guidelines for ^{177}Lu SPECT quantitative imaging established using the SIMIND (Simulating Medical Imaging Nuclear Detectors) MC program [41]. However, this document does not report the quantification accuracy or error obtained with the recommended methods. Each clinic should thus determine the quantification error relevant for their chosen setup and method. There is increasing evidence supporting the need for personalized dosimetry based on SPECT quantitative information. The attempt has been hindered by the lack of standardized methods, which include determining the gamma camera CF. As indicated in the above studies, there is no consensus with regard to the CF geometry. Wevrett et al. demonstrated the feasibility of using simple phantom geometries to standardize gamma camera calibrations for activity quantification of ^{177}Lu and ^{131}I [42]. These phantom geometries included a sphere placed centrally in air and in water as well as at an offset of 8.6 cm in water. The authors concluded that none of their geometries were sufficient to be used individually and recommended that a mean value obtained from the different geometries should be incorporated. They also suggested that the characterization of the change in the CF with lesion volume was necessary due to the PVE and have proposed that the CF and RC should be combined in a mean calibration coefficient. This approach may require that a large range of CF values be determined from different geometries and tabulated. In addition, the CF would be affected by the VOI definition and further affected by the segmentation method used to determine the RC. In another publication, Wevrett et al. assessed the feasibility of carrying out an international inter-comparison of European hospitals to determine the consistency of the CFs used at these sites [43]. In the exercise dual compartment spherical sources of known activity concentration and volume, were sent to seven hospitals and acquired in a

water-filled Jaszczak phantom. The hospitals acquired and processed the data using their own choice of methods. The authors reported that no single method reported by the different hospitals yielded significantly improved accuracy. Further research has to be carried out to investigate the uncertainties associated with determining a suitable CF for ^{177}Lu SPECT quantitative imaging.

In this study, we aimed to investigate the effect of two CF geometries and their corresponding RCs on the quantification accuracy of ^{177}Lu SPECT images using MC simulations. The CFs were obtained from (i) a radioactive sphere surrounded by non-radioactive water, termed sphere-CF, and (ii) a cylindrical phantom uniformly filled with radioactive water, termed a cylinder-CF. Two sets of RC curves were generated as a function of object size, using the two CFs. The first RC curve was constructed using the sphere-CF and the second RC curve was created using the cylinder-CF; the two curves were used to obtain the sphere-RC and cylinder-RC values, respectively. The effects of the sphere-CF-RC and cylinder-CF-RC combinations, on the quantification accuracy of ^{177}Lu activity derived from SPECT images, were evaluated using three phantom geometries.

2. Materials And Methods

The SIMIND MC program (SIMIND version 6.1.2) was used in this study. Its ability to successfully mimic ^{177}Lu SPECT images with a model of a Siemens Symbia T16 hybrid SPECT/CT (Symbia T16) (Siemens Medical Solutions, Inc. Hoffman Estates, IL., USA) dual-head gamma camera was validated in a previous study [44]. Details describing the gamma camera physical parameters were as defined in the above-mentioned publication. Three voxelized phantoms, as shown in Fig. 1, were used in this study. They were created by segmenting the CT images of these phantoms with the software ITK-snap (version 3.2.0) [45] as described in detail by Ramonaheng et al. [44]. The three phantoms shown in Fig. 1 were: (a) a cylindrical phantom with a segmented volume of 9 900 ml, (b) an RSD Alderson torso phantom (Radiological Support Devices Inc, USA) which was segmented to isolate the lung inserts (combined segmented volume of 2 090 ml), the liver insert (1 090 ml) and the remainder of the phantom (2 095 ml), and (c) a randomly selected SPECT/CT patient study anonymously obtained from the Symbia T16 patient database, approved by our institution's ethics committee. For the patient phantom, the liver (1 590 ml), lungs (2 270 ml), spleen (160 ml), left (159 ml) and right (169 ml) kidneys, as well as the remaining volume of the patient (14 100 ml), were segmented. Each of the voxelized phantoms was appropriately equipped with spherical inserts using ITK-snap to mimic tumors.

The simulations were set up for ^{177}Lu using a medium-energy (ME) collimator with a 20% energy window centered over the 208 keV photopeak (187.2 – 228.8 keV) [19,46–48]. For all SPECT simulations, the phantoms were placed in the center of the field of view and projection data were simulated over 360° with equally spaced projections using a non-circular orbit. The phantom to detector distance was determined for each projection angle using a density map to mimic auto-contour detection of the phantom outline [44]. All simulations were conducted with a high number of photon histories to ensure data sets with low

simulation noise. Sixty (60) projections with an equivalent of 45 s acquisition time were simulated and the image data were stored in a 128 × 128 matrix with a pixel size of 4.8 × 4.8 mm [16,49].

Our study comprised two phases. The *first phase* of the study focused on three essential steps required to optimize the reconstruction parameters and the quantification process. The steps consisted of (i) optimizing the 3D OS-EM reconstruction algorithm, (ii) establishing the CFs and (iii) determining the RCs. The *second phase* of the study evaluated the quantification accuracy, reported as the quantification error, achieved with the steps established in the initial phase by quantifying spherical inserts in the three above-mentioned phantoms. The kidney quantification in the patient phantom was also evaluated. The simulations of the phantoms comprised simulated projection images and result files describing the simulation protocol. A 3D OS-EM algorithm was used for image reconstruction and employed CT-based attenuation correction, ESSE scatter correction [28,50], and CDR correction. The CDR correction included modelling of the intrinsic and geometric response as well as the septal penetration and septal scatter. All the reconstructed data were analyzed using the public domain software Amide [51]. Spherical volumes corresponding to the physical sizes of the spheres were used to delineate all the spheres. This method of delineation is analogous to the use of CT images for segmentation of quantitative SPECT images [15,52,53]. Due to the irregular shape of the kidney, a 3D-isocontour threshold method was used to delineate the kidney volumes. The minimum and maximum threshold values were chosen to result in the equivalent volume of each kidney as obtained from the simulation results. The mean counts from the fractional voxels were used to calculate the total counts from these VOIs.

- **Quantification steps**

For the first phase of the study, each of the phantom geometries in the quantification steps was simulated with a uniform ^{177}Lu concentration of 3.04 MBq/ml. This is comparable to concentrations reported in the literature for similar investigations [54]. Different sphere sizes were simulated individually in the center of the phantom to avoid spill-in of nearby spheres.

- ***3D OS-EM optimization***

To determine the optimal number of 3D OS-EM updates required for convergence (where 90% of the true activity is recovered), SPECT images of a cylindrical phantom equipped with radioactive spheres with volumes (and their corresponding diameters) of 4.0 ml (2.0 cm), 14.1 ml (3.0 cm) and 65.4 ml (5.0 cm) in a warm background were simulated. To further investigate the effect of the sphere-to-background ratio on the convergence, each sphere was simulated using sphere-to-background ratios of 6:1 and 13:1 [52,54,55]. The reconstruction was performed as described above and multiple 3D OS-EM updates (ranging from 24 to 192) were used. As the quantified activity for the spheres is not yet known, the total counts for each sphere size were normalized to the maximum number of counts obtained at 192 updates for each particular VOI, and expressed as percentage recovery. The aforementioned percentage recovery for each sphere was plotted as a function of the number of updates. The optimization process was repeated with a clinical geometry by simulating the left and right kidneys of the patient. Similarly, the

kidney-to-background ratios and concentrations were equivalent to those used for the spheres. The convergence, needed for high reconstruction accuracy for both the sphere and kidneys, was defined as the 90% recovery [26].

- ***Calibration factors***

The sphere-CF was calculated using a simulation of a 65.4 ml (5.0 cm) radioactive sphere placed in the cylindrical phantom (Fig. 1(a)) with a non-radioactive background. The sphere diameter was selected to be more than three times the system spatial resolution to limit the influence of PVE on the accuracy of activity quantification. The system spatial resolution for the ^{177}Lu 208 keV photopeak using a ME collimator was determined in a previous study, resulting in a FWHM of 1.1 cm [44]. The cylinder-CF was calculated using a simulation of the above-mentioned cylindrical phantom filled with a uniform activity distribution. Both geometries offered simple scatter and attenuation properties that could be used to minimize the effect of imperfect corrections. Considering that ^{177}Lu is a costly therapeutic isotope, with a relatively long physical half-life of 6.7 days, the non-radioactive background of the sphere-CF offered a more practical alternative that could easily be implemented in clinical practice compared to the cylinder-CF. The CFs were calculated using the general formula shown in Eq. 1.

$$CF\ (cps/MBq) = \frac{CR\ (cps)/V\ (ml)}{TC\ (MBq/ml)} \qquad (1)$$

- ***Recovery coefficients***

The RCs for partial volume compensation were obtained from simulated SPECT images of the cylindrical phantom uniformly filled with; ^{177}Lu and radioactive spheres with known concentration of varying sizes, below and above the known system spatial resolution. The sphere volumes used were 2.4 ml (1.5 cm), 4.2 ml (2.0 cm), 8.2 ml (2.5 cm), 14.1 ml (3.0 cm), 22.4 ml (3.5 cm), 33.5 ml (4.0 cm), 47.7 ml (4.5 cm) and 65.4 ml (5.0 cm) with a sphere-to-background ratio of 6:1. The concentration was calculated using the sphere-CF and the cylinder-CF and expressed as a fraction of the true concentration (Eq. 2) to determine the RC of the sphere and cylinder respectively.

$$RC = \frac{C_{cal}}{C_{true}} \qquad (2)$$

where *RC* is the recovery coefficient, C_{cal} and C_{true} are the calculated and true activity concentrations (MBq/ml) in the spheres respectively. The values of the coefficients from the curve function shown in Eq. 3 were determined by fitting a mono-exponential function (Eq. 3) to the above-mentioned sphere and cylinder RC data to generate the sphere-RC and cylinder-RC values used for PVC.

$$y = a - b(e^{-cx}) \qquad (3)$$

where *y* indicates the required RC value, *x* is the sphere diameter and *a*, *b*, and *c* are the fitting constants. The application of sphere-based RC curves (look-up tables) for PVC of the kidneys based solely on volume dependence has been reported to be non-optimal for ^{177}Lu SPECT/CT image quantification [29]. This was due to the differences found between the renal RCs and sphere-RCs. The authors suggested the replacement of sphere based RCs with geometry specific RC look-up tables for the kidneys. Therefore, instead of applying a volume dependent RC value based on the fitted functions of the spheres, we opted to calculate the RC values for the sphere-RC and cylinder-RC using Eq. 2 directly. The generation of geometry specific look-up tables using kidneys of different volumes was beyond the scope of this study and the calculation of the kidney RC values in the above-mentioned manner seemed to be the better choice. The sphere-RC and cylinder-RC values, for the different size spheres and the kidneys used for PVC in the subsequent sections, were tabulated with their percentage differences.

- **Evaluation of quantification accuracy**

The second phase of the study evaluated the ^{177}Lu SPECT quantification error in the three phantoms. The objective of the first phantom (cylindrical phantom) was to determine the ^{177}Lu quantitative error of the spherical inserts in a phantom which characterized a simple homogeneous attenuating geometry. The second phantom (torso phantom) represented a more complex non-homogeneous attenuating geometry and the third phantom (patient phantom) extended the quantification error to a clinically realistic phantom. All the phantoms were simulated four times with inclusion of one of the spheres of volume: 15.6 ml (3.1 cm), 24.4 ml (3.6 cm), 33.5 ml (4.0 cm) and 65.4 ml (5.0 cm) on each simulation respectively. The sphere concentrations were 2.2 MBq/ml with a sphere-to-background ratio of 13:1. The sphere-to-background ratio selected for the simulations of the three phantoms was slightly different to those simulated for the RC (6:1) to avoid biased results in the determination of the quantification error. Each sphere was simulated in the center of the cylindrical phantom as well as in the abdomen next to the liver for the torso and patient phantoms. The relative concentration in the various structures found in these two phantoms was defined to reflect typical activity distribution of ^{177}Lu-DOTATATE [49,56]. The torso phantom had lung and liver concentrations of 0.34 MBq/ml and 0.51 MBq/ml, respectively (similar to the patient phantom), with a background concentration of 0.17 MBq/ml. For the patient phantom, the concentration for the spleen was 0.52 MB/ml, with corresponding kidney and background concentrations of 0.45 MBq/ml and 0.02 MBq/ml, respectively. The kidney-to-background ratio of 23:1 for the patient phantom reflected a 24-hour uptake for a ^{177}Lu-DOTATATE pharmacokinetic study [49].

Two sets of quantification results were obtained for each of the phantoms. Firstly, the counts were converted to concentration using the sphere-CF without PVC to generate the sphere-CF quantification error, and subsequently corrected for partial volume using the corresponding sphere-RC to generate a sphere-CF-RC quantification error. Secondly, the counts were converted to concentration using the cylinder-CF without PVC to obtain the cylinder-CF results and the cylinder-RC applied for PVC, resulting in the cylinder-CF-RC data. The quantification error was calculated as the percentage difference between the

true concentration used as input into SIMIND and the quantified concentration calculated from the images (Eq. 4).

$$Quantification\ Error\ (\%) = \frac{Quantified\ (MBq/ml) - True\ (MBq/ml)}{True\ (MBq/ml)} \times 100 \qquad (4)$$

3. Results

3.1 Quantification steps

3.1.1 3D OS-EM optimization

The effect of the number of 3D OS-EM updates on the percentage recovery is illustrated in Fig. 2. The percentage recovery values were calculated from the reconstructed ^{177}Lu SPECT images of three different sized spheres simulated in a cylindrical phantom, as well as the left and right kidneys of the patient phantom. The recovery values in Fig. 2 (a) and (b) were derived from simulations when the object-to-background ratios of 13:1 and 6:1 were used. The total counts obtained for each VOI were normalized to the maximum counts of the 3D OS-EM updates and expressed as a percentage recovery.

As seen in Fig. 2, fewer updates were required for the larger objects to reach convergence (count recovery > 90%). Convergence was reached for the right and the left kidney as well as the 65 ml sphere after only 24 updates. In contrast, the 14 ml and the 4.2 ml spheres achieved 90% recovery only after 48 and 84 updates, respectively. These observations applied to both concentration ratios in Fig. 2 (a) and (b).

3.1.2 Calibration factors

The results for the sphere-CF and the cylinder-CF were 13.9 cps/MBq and 16.3 cps/MBq, respectively. The sphere-CF underestimated the cylinder-CF by 16.3%. The results demonstrated that the VOI drawn based on the physical dimensions of the sphere excluded some of the counts for the sphere-CF due to spill-out. As a result, a lower CF value was obtained for the sphere-CF in comparison to that of the cylinder-CF.

3.1.3 Recovery coefficients

Figure 3 shows the characteristic non-linear curves fitted with R^2 values of 0.99, generated using the sphere-CF and cylinder-CF, when RC values were plotted for the different sphere sizes, allowing for interpolation between the sphere sizes. The curves provided the fraction of ^{177}Lu activity concentration recovered from the reconstructed images for the given sphere sizes, and in so doing allowed for the true concentration to be calculated, thus compensating for PVE. Although the simulated concentrations (C_{true}) were the same for all VOIs, the smaller spheres had lower calculated concentration (C_{cal}) values, demonstrating the PVE. It is evident from these curves that RC is strongly dependent on the size of the spheres.

The sphere-RC and cylinder-RC for the spheres and kidneys are summarized in Table 1. The RC values ranged from 0.77 to 1.00 as the size of the sphere increased from 16 ml to 65 ml. The kidney RC values were 1.18 and 0.99 for the sphere-RC and cylinder-RC, respectively. Table 1 demonstrates that there is a constant difference between the sphere-RC and the cylinder-RC values for all the simulated objects. The average sphere-RC value overestimated the average cylinder-RC value by 16.3 ± 0.04%, which may be attributed to the CF difference reported in Table 1.

Table 1 The recovery coefficient (RC) values for the sphere and kidney volumes generated for the sphere and cylinder calibration factors (CFs)

Objects	Sphere-RC	Cylinder-RC	% difference
Kidneys			
L-K: 159 ml	1.18	0.99	16.3
R-K: 169 ml	1.18	0.99	16.3
Spheres			
16 ml	0.92	0.77	16.3
24 ml	0.96	0.81	16.3
34 ml	0.98	0.82	16.3
65 ml	1.00	0.84	16.4
		Average	**16.3 ± 0.04**

L-K, left kidney; *R-K*, right kidney; *RC*, recovery coefficient

3.2 Evaluation of quantification accuracy

Cylindrical phantom

Table 2 shows the quantification error results for the spheres simulated in the cylindrical phantom with and without PVC. The results were calculated using the sphere-CF and cylinder-CF without PVC, while the combinations of sphere-CF-RC and cylinder-CF-RC were applied to compensate for the PVE.

Table 2 Quantification error results for spheres simulated in a cylindrical phantom with and without partial volume corrections (PVCs)

	Quantification error (%)			
Object	**Without PVC**	**With PVC**	**Without PVC**	**With PVC**
Sphere	Sphere-CF	Sphere-CF-RC	Cylinder-CF	Cylinder-CF-RC
16 ml	-4.56	3.32	-20.08	3.28
24 ml	-3.40	0.19	-19.11	0.19
34 ml	-2.05	-0.43	-17.98	-0.43
65 ml	1.60	0.83	-14.93	0.86
Average	**-2.10 ± 2.67**	**0.98 ± 1.64**	**-18.03 ± 2.23**	**0.98 ± 1.62**

CF, calibration factor; *PVC*, partial volume correction; *RC*, recovery coefficient

As seen in Table 2, the trend for the quantification error without PVC was as expected. The smallest sphere showed the largest quantification error, demonstrating the influence of PVEs, which was less important with increasing sphere size. The average quantification error obtained with the sphere-CF without PVC was -2.10 ± 2.67% in comparison to that obtained with the cylinder-CF by a value of -18.03 ± 2.23%. The use of the cylinder-CF without PVC underestimated the true activity evidently for all the sphere sizes. PVC improved the average quantification error dramatically from -18.03 ± 2.23% to 0.98 ± 1.62% for the cylinder results. The precision (standard deviation) of the average quantification error improved slightly with PVC for both the sphere and cylinder data. A slight overestimation (≤ 3.32%) of the activity values was observed for both phantoms for the smallest spheres when PVC was applied. The use of the sphere-CF-RC and cylinder-CF-RC resulted in comparable average quantification errors of 0.98 ± 1.64% and 0.98 ± 1.62%, respectively.

Torso phantom

The quantitative error results obtained for the spheres simulated in the torso phantom are demonstrated in Table 3. Similar to the cylindrical phantom, the results were analyzed using the two sphere-CF and cylinder-CF without PVC, and the corresponding sphere-RC and cylinder-RC were applied to correct for partial volume.

Table 3 Quantification error results for spheres simulated in the torso phantom with and without partial volume corrections (PVCs)

	Quantification error (%)			
Object	**Without PVC**	**With PVC**	**Without PVC**	**With PVC**
Sphere	Sphere-CF	Sphere-CF-RC	Cylinder-CF	Cylinder-CF-RC
16 ml	-4.92	2.92	-20.39	2.99
24 ml	-5.54	-2.03	-20.90	-2.03
34 ml	-4.84	-3.26	-20.32	-3.26
65 ml	-2.70	-3.44	-18.53	-3.41
Average	**-4.50 ± 1.24**	**-1.45 ± 2.98**	**-20.04 ± 1.04**	**-1.43 ± 3.01**

CF, calibration factor; *PVC*, partial volume correction; *RC*, recovery coefficient

Without PVC, the quantification error showed an average underestimation of 4.50 ± 1.24% for the sphere-CF. Similar to the sphere quantification results in the cylindrical phantom; the cylinder-CF considerably underestimated the quantified concentration, with an absolute average of 20.04 ± 1.04% for all sphere sizes.

It can be seen from the results in Table 2 and Table 3 that the calculated concentration underestimated the true concentration to the same extent between the two phantoms, with the worst quantification results obtained when applying the cylinder-CF with no PVC. Partial volume correction for both the sphere and cylinder slightly overestimated the concentration of the two smallest spheres (≤ 2.99%). Analogous to the sphere quantification in the cylindrical phantom, the application of the sphere-CF-RC and cylinder-CF-RC resulted in comparable average quantification errors of -1.45 ± 2.98% and -1.43 ± 3.01%, respectively.

Patient phantom

Figure 4 shows the patient phantom reconstructed SPECT data with its associated CT data illustrating the sphere and the kidney objects (indicated by the arrows) used for quantification analysis. Table 4 compares the quantification errors obtained for the spherical and kidney objects simulated in the patient phantom calculated using the sphere and the cylinder data.

As seen from Table 4, the sphere quantification errors showed similar trends to those obtained in the cylindrical and torso phantoms. A small average quantification error of -0.93 ± 2.97% was obtained when applying the sphere-CF without PVC in the patient phantom. Partial volume correction using the sphere-CF-RC altered the average quantification error to 2.18 ± 0.91%. These results were comparable to those obtained in the torso (-1.45 ± 2.98%) and the cylindrical phantom (0.98 ± 1.64%). The cylinder-CF underestimated the absolute average quantified concentration of the spheres (17.07 ± 2.48%) similar to the torso (20.04 ± 1.04%) and the cylindrical phantom (18.03 ± 2.23%). Partial volume correction

improved the cylinder-CF-RC to an average of 2.20 ± 0.94% similar to the torso (-1.43 ± 3.01%) and cylindrical phantom (0.98 ± 1.62%). When all corrections were applied, the sphere-CF-RC (2.18 ± 0.91%) was comparable to the cylinder-CF-RC (2.20 ± 0.94%) data, validating findings of the cylindrical and torso phantoms.

Table 4 Quantification error results for the spherical and kidney objects simulated in the patient phantom calculated with and without partial volume corrections (PVCs)

	Quantification error (%)			
Objects	**Without PVC**	**With PVC**	**Without PVC**	**With PVC**
Spheres	Sphere-CF	Sphere-CF-RC	Cylinder-CF	Cylinder-CF-RC
16 ml	-4.42	3.47	-19.97	3.53
24 ml	-1.70	1.95	-17.69	1.94
34 ml	-0.34	1.32	-16.65	1.32
65 ml	2.73	1.96	-13.98	1.99
Average	**-0.93 ± 2.97**	**2.18 ± 0.91**	**-17.07 ± 2.48**	**2.20 ± 0.94**
Kidneys				
L-K: 159 ml	18.98	1.01	-0.37	0.94
R-K: 169 ml	22.34	3.50	2.44	3.45
Average	**20.66 ± 2.38**	**2.26 ± 1.76**	**1.04 ± 1.99**	**2.20 ± 1.77**

CF, calibration factor; *L-K*, left kidney; *PVC*, partial volume correction; *R-K*, right kidney; *RC*, recovery coefficient

The kidney quantification showed an average overestimation of 20.66 ± 2.38% for the sphere-CF without PVC, in comparison to the better results (1.04 ± 1.99%) obtained for the cylinder-RC. This was contrary to the sphere quantification results where a considerable underestimation of the quantification error was obtained using the cylinder-CF without PVC. The kidney quantification error improved to 2.26 ± 1.76% with the sphere-CF-RC corrections. With PVC the sphere-CF-RC and cylinder-CF-RC yielded comparable average quantification results of 2.26 ± 1.76% and 2.20 ± 1.77%, respectively; similar to the findings of the sphere quantification results. The results suggest that PVC did not play a major role in the kidney quantification error using the cylinder data. This may be attributed to the fact that the cylinder-RC value applied to the kidneys was close to 1.0.

4. Discussion

4.1 Quantification steps

4.1.1 3D OS-EM optimization

The trends observed in Fig. 2 (a) and (b) were similar, and convergence (recovery ≥ 90%) was observed at 84 updates for all the objects indicated by the 90% dashed line. Although better reconstruction accuracy, beyond the 90% recovery, could be reached at higher updates, the following was taken into consideration. A higher number of updates increased the number of recovered counts, but has also been shown to increase image noise levels which may obscure the VOI delineation [27, 57]. In addition, the use of CDR compensation in the reconstruction process has been shown to result in pronounced edge ringing artefacts with an increased number of iterations, particularly for larger objects [58, 59]. The reconstruction computational times are longer with increased updates, which is an important consideration for practical implementation. Keeping in mind the above-mentioned literature findings, 84 updates for image reconstruction were considered sufficient to attain a 90% recovery for all investigated object sizes. These finding were in par with Brolin et al. [49] and Ljungberg et al. [16] who used a total of 80 3D OS-EM updates for quantification of ^{177}Lu-DOTATATE distribution. Therefore, the 84 updates were used for reconstruction of the subsequent data of this study.

4.1.2 Calibration factors

The underestimation of the sphere-CF in comparison to the cylinder-CF value was attributed to PVE due to spill-out of counts. Some authors have suggested the simple use of an additional 3 cm margin to the physical dimensions of the sphere to include spilled-out counts [39]. Other authors have defined VOIs according to the physical dimensions of the CF sphere [60] or bottles [15] for quantification of ^{177}Lu SPECT studies. We found purpose in defining the sphere-CF VOI as the physical dimensions of the sphere in order to have a consistent delineation method for the quantified spheres. The 65 ml sphere was chosen to limit PVEs, however, the comparative assessment between the cylinder-CF and the sphere-CF indicated that spill-out counts from the sphere were not completely eliminated for but were reduced. The cylinder VOI was selected centrally on the cylinder image where the effects of spill-in and spill-out of count were presumed to cancel. Several ^{177}Lu SPECT CF values obtained with the 208 keV photopeak window and a ME collimator with corrections for attenuation, scatter and CDR have been reported in literature. These values differ vastly depending on the phantom configurations, VOI definition, the gamma camera used, and the types of corrections applied to the data. A value of 20.2 cps/MBq for a cylindrical phantom with a VOI containing the entire phantom are reported for a Siemens Symbia Intevo Bold SPECT/CT system (Siemens Healthineers, Germany) [29]. The same authors reported values of 18.86 cps/MBq and 20.36 cps/MBq for VOIs drawn centrally in the cylindrical phantom and that encompassing the entire phantom [61]. While other authors have reported values of 10.1 cps/MBq and 10.3 cps/MBq for the Symbia T16 (Siemens Healthineers, Germany) obtained using a cylindrical phantom and by applying a 50% threshold of the maximum voxel value to define the VOI for the CF [62]. Mean CF values (simulated for different

gamma cameras) of 10.5 cps/MBq, 9.5 cps/MBq and 10.1 cps/MBq, for phantom geometries, which included a sphere in a non-radioactive background, a sphere in a radioactive background and a uniform cylindrical phantom, respectively, have been reported [40]. The above variations illustrate the variability obtained with the different gamma cameras, processing software, phantom geometries and VOI definitions, emphasizing the need to establish a CF suitable for a specific SPECT quantification study.

4.1.3 Recovery coefficients

The intention of creating sphere-RC and cylinder-RC curves was to obtain approximate RC values for spherical objects of different sizes where spill-out of counts were present and when PVC is required. In order to use sphere-RC and cylinder-RC curves from Fig. 2 for PVC, the physical size of the sphere is needed and may be obtained from the CT image of the study. The constant difference between the sphere-RC and the cylinder-RC was demonstrated by the average difference of 16.3 ± 0.04%. The results were consistent for both the spheres and the kidneys. The discrepancy was attributed to the differences between the two CFs used to calculate the RCs. The overestimation of the sphere-RC served as compensation for the underestimation of the sphere-CF and vice versa for the cylinder-RC and cylinder-CF. The cylinder-RC value of 0.81 for the 24 ml sphere was comparable to the 0.85 RC value reported by Hippeläinen et al. [15] for a 26 ml sphere. Similarly, Sanders et al. [60] reported a RC value of 0.80 for a 16 ml sphere compared to our 0.77 value for the same size sphere. Our study contained spherical objects mimicking tumors, and therefore PVC using curves from Fig. 2 may be applicable if the object in the phantom has a similar configuration. The RCs may differ if the shape of the object has an irregular shape, or a non-uniform activity distribution [29]. For this reason, the kidney RC values were calculated directly using Eq. 2 and not from the fitted RC curves. This method is applicable when the size and activity concentration of the object are known. The size of the objects may be obtained from high resolution images such as CT or MRI.

4.2 Evaluation of quantification accuracy

The sphere quantification error results (Table 2 to Table 4) obtained with the sphere and cylinder CF and RC data showed similar trends for all three phantoms. The slight overestimation of the activity values observed for the smallest sphere (16 ml) when PVC was applied for both the sphere and cylinder data may be attributed to the discrepancy between the calculated RC value and that obtained from the fitted function shown in Fig. 2. It can be seen from Fig. 2 that the function slightly underestimated the calculated sphere-RC and cylinder-RC values at a sphere diameter of 3 cm, comparable to the diameter of the smallest quantified sphere (3.1 cm). The sphere-CF without PVC showed a general tendency of a small quantification error for the quantified spheres compared to the large underestimation by the cylinder-CF. This may be expected due to the similar geometry between the quantified spheres and the sphere used for the sphere-CF. These results illustrated the dependence of the quantified error on the geometry of the CF. Whole-organ specific CFs, obtained using 3D printed phantom inserts in the shape of the spleen, kidney, pancreas and liver, have shown to improve the accuracy of organ dosimetry for ^{99m}Tc and ^{177}Lu SPECT studies [52]. This type of dependence was verified in our study by extending the quantification error evaluation to a clinical kidney geometry. Without PVC a large overestimation of the

quantified kidney concentration for the sphere-CF was obtained vs. the small kidney quantification error obtained with the cylinder-CF. The VOI selection for the sphere-CF and cylinder-CF resulted in differences in the contribution of spill-in and spill-out of counts due to the PVE. The different effects of the two CFs were balanced by their corresponding RC values. This was shown by the comparable average quantification error results obtained for the different sized spheres in all three phantoms as well as the kidneys in the patient phantom.

The quantification errors obtained in this study compared well with literature investigations of similar phantom geometries. De Nijs et al. [55] investigated the ^{177}Lu SPECT activity quantification of radioactive spherical inserts placed in a cylindrical phantom with radioactive background and reported errors of 10% for their largest sphere (37 ml). Sanders et al. [60] reported larger errors of 20% for smaller sphere inserts (16 ml) in the same geometry. An average percentage error of 6.6 ± 3.5% for quantification of 175 ml cylindrical inserts placed in a larger cylinder was reported by Beauregard et al. [46]. Therefore, the quantification errors (≤ 0.98 ± 1.64%) found for the cylindrical phantom used in our study were satisfactory when all corrections were applied. Hippeläinen et al. [15] investigated the ^{177}Lu SPECT activity quantification of spheres measured in the same torso phantom and reported errors of 15% for their largest spherical insert (104 ml). The quantification errors found in our study (≤ -1.43 ± 3.01%) were comparable to that of D'Arienzo et al. [63] who quantified a cylindrical insert (19.13 ml) in an anthropomorphic torso phantom with an accuracy of 2.0%, and Uribe et al. [54] who reported accuracies of < 5.0% for their largest insert (34 ml) in a thorax phantom. Beauregard et al. [46] reported quantification error results of 2.6 ± 1.8% for ^{177}Lu SPECT activity data of five patients acquired with the Symbia TruePoint T6 SPECT/CT gamma camera (Siemens, Healthineers, Germany). The authors evaluated their quantification error by comparing the calibrated activity injected into the patients with the quantified activity obtained by drawing a VOI surrounding the patient using CT images. Although their quantification method varied, their results were comparable to our patient phantom findings when all corrections were applied with sphere and kidney quantification errors of ≤ 2.20 ± 0.94% and ≤ 2.26 ± 1.76%, respectively. Sanders et al. [60] compared ^{177}Lu bladder activity concentrations obtained from SPECT/CT patient images with urine sample measurements from calibrated well counters and yielded mean quantification errors of 10 ± 8.3%. Bailey et al. [14] has reported accuracies of ± 10% for ^{177}Lu activity quantification of whole body planar scans and cardiac blood pool SPECT images. Hippeläinen et al. [15] reported errors of up to 25% for kidney quantification of patients who underwent ^{177}Lu-DOTATATE treatment using SPECT images. The systematically higher activity quantification errors were attributed to the estimates obtained at different time points. Willowson et al. [53] investigated the accuracy of using a single time point for renal dosimetry and showed improvement in the quantification accuracy to 13% and 2% when using the 4-hour and 24-hour data only. Optimization of kidney quantification for ^{177}Lu SPECT/CT using geometry specific RCs for PVC was investigated using a 3D printed two compartment kidney phantom [29]. The best quantification accuracies of 1.5% and 10.3% were reported using the commercially available reconstruction algorithms xSPECT and Flash-3D (Siemens, Healthineers, Germany), respectively, when model-based RCs were applied to compensate for PVE. These studies demonstrate the disparity in quantitative accuracy found for the different imaging geometries processing protocols and methods

evaluating the quantitative error. The overall improved quantitative results obtained in our study when all corrections are applied may be indicative of the accuracy of the correction methods used in the reconstruction process. The ESSE model-based scatter correction used in this study has been reported to be more accurate for scatter correction of ^{177}Lu data compared to window-based methods [55].

5. Conclusion

In this study, we used the SIMIND MC program to model a Siemens Symbia T16 gamma camera for ^{177}Lu SPECT imaging of voxelized phantoms as validated by Ramonaheng et al. [44]. Emanating from the fact that there is currently no consensus on the ideal SPECT CF geometry for quantitative data, we presented two CFs and their corresponding RCs. The quantification errors obtained with the two-combination sphere-CF-RC and cylinder-CF-RC were evaluated by quantifying different size spheres in three different phantom geometries as well as the kidneys in the patient phantom. Our study showed the effect on the quantification error by using the sphere-CF or the cylinder-CF without PVC is dependent on the quantified geometry. The quantification results emphasized the importance of applying a PVC with an RC obtained with the same CF used to convert the quantified data into units of concentration. We demonstrated that when all corrections were applied (attenuation, scatter, CDR and partial volume), the ^{177}Lu SPECT quantification errors in the three phantoms were comparable for the sphere-CF-RC and cylinder-CF-RC combinations. Our absolute quantification errors of smaller than and equal to 3.53% for the three phantoms, compared well to literature findings and complied with the ± 5% absorbed dose accuracy required for molecular radiotherapy [64]. Although our findings suggest the feasibility of obtaining accurate ^{177}Lu SPECT activity quantification upon the careful selection of a CF-RC combination, certain considerations may be limiting. These include firstly, that the application of patient specific RCs in the clinic entails the use of CT or MRI data in combination with MC simulations. This would require modelling of CF-RC combinations for every patient geometry and activity distribution, which may be cumbersome to implement routinely. Secondly, the presence of non-uniform activity distributions may further complicate activity quantification. This study reinforces the need to standardize segmentation methods for CF, RCs and tumor and organ delineation.

List Of Abbreviations

CDP - collimator detector response; CF - calibration factor; DEW - dual energy window; ESSE - effective source scatter estimation; FWHM - full-width half-maximum; MC - Monte Carlo; ME - medium-energy; OS-EM - ordered subset expectation maximization; PRRT - peptide receptor radionuclide therapy; PVC - partial volume correction; PVE - partial volume effect; RC - recovery coefficient; TEW - triple energy window; VOI - volume of interest

Declarations

Funding

This work was funded by the Science and Technology Research Collaboration between the National Research Foundation of South Africa (NRF), and the Swedish Foundation for International Cooperation in Research and Higher Education (STINT), grant STINT 160811184621. Partial financial support was received from NTeMBI (Necsa).

Competing interests

The authors declare that they have no competing interests.

Ethics approval

This study was performed with approval from the Health Sciences Research Ethics Committee at the University of the Free State, Ethics number UFS-HSD2019/1506/0110. The HSREC functions in compliance with, but not limited to, the following documents and guidelines: The SA National Health Act. No. 61 of 2003; Ethics in Health Research: Principles, Structures and Processes (2015); SA GCP(2006); Declaration of Helsinki; The Belmont Report; The US Office of Human Research Protections 45 CFR 461 (for non-exempt research with human participants conducted or supported by the US Department of Health and Human Services- (HHS), 21 CFR 50, 21 CFR 56; CIOMS; ICH-GCP-E6 Sections 1-4; The International Conference on Harmonization and Technical Requirements for Registration of Pharmaceuticals for Human Use (ICH Tripartite), Guidelines of the SA Medicines Control Council as well as Laws and Regulations with regard to the Control of Medicines, Constitution of the HSREC of the Faculty of Health Sciences at UFS.

Consent to participate

Not applicable.

Consent for publication

Not applicable.

Availability of data and material

The datasets generated during and/or analyzed during the current study are available from the corresponding author on reasonable request.

Code availability

The Monte Carlo simulation code (SIMIND) and the OS-EM reconstruction software was made available by Prof. Michael Ljungberg from the Department of Medical Radiation Physics at the University of Lund, Sweden.

Authors' contributions

KR was responsible for all the simulations, reconstruction, segmentations, data analysis, writing the original manuscript and participated in the study design, conceptualization and editing with JVS and HdR. JvS was responsible for the software implementation. JvS and HdR were responsible for the review, project administration, supervision and funding acquisition. All authors read and approved the final manuscript.

Acknowledgments

The authors acknowledge the Department of Nuclear Medicine at Universitas Academic Hospital in Bloemfontein, Free State, South Africa, for permission to use the equipment. We wish to express our gratitude to Prof. M. Ljungberg from the Department of Medical Radiation Physics at the University of Lund, Sweden, for making the OS-EM reconstruction algorithm that is part of Lundadose dosimetry software, freely available to us and for his technical support. We also thank Ms. M. Morphis for her technical assistance with the software. We thank Prof. W.I.D. Rae from the Department of Medical Radiation Science at the University of Sydney for editing the manuscript and Ms. T. Mulder, medical editor at the Faculty of Health Sciences, University of the Free State, South Africa, for technical and editorial preparation of the manuscript.

References

1. Bodei L, Mueller-Brand J, Baum RP, Pavel ME, Hörsch D, O'Dorisio MS, et al. The joint IAEA, EANM, and SNMMI practical guidance on peptide receptor radionuclide therapy (PRRNT) in neuroendocrine tumours [published correction appears in Eur J Nucl Med Mol Imaging. 2014 Mar;41(3):584. O'Dorisiol, TM [corrected to O'Dorisio, TM]]. Eur J Nucl Med Mol Imaging. 2013;40(5):800–16. https://doi.org/10.1007/s00259-012-2330-6

2. Volkert WA, Goeckeler WF, Ehrhardt GJ, Ketring AR. Therapeutic radionuclides: production and decay property considerations. J Nucl Med. 1991;32(1):174–85.

3. Banerjee S, Pillai MR, Knapp FF. Lutetium-177 therapeutic radiopharmaceuticals: linking chemistry, radiochemistry, and practical applications. Chem Rev. 2015;115(8):2934–74. https://doi.org/10.1021/cr500171e

4. Dash A, Pillai MR, Knapp FF Jr. Production of ^{177}Lu for Targeted Radionuclide Therapy: Available Options. Nucl Med Mol Imaging. 2015;49(2):85–107. https://doi.org/10.1007/s13139-014-0315-z

5. Bodei L, Cremonesi M, Ferrari M, Pacifici M, Grana CM, Bartolomei M, et al. Long-term evaluation of renal toxicity after peptide receptor radionuclide therapy with ^{90}Y-DOTATOC and ^{177}Lu-DOTATATE: the role of associated risk factors [published correction appears in Eur J Nucl Med Mol Imaging. 2008 Oct;35(10):1928]. Eur J Nucl Med Mol Imaging. 2008;35(10):1847–56. https://doi.org/10.1007/s00259-008-0778-1

6. Bodei L, Cremonesi M, Grana CM, Fazio N, Iodice S, Baio SM, et al. Peptide receptor radionuclide therapy with ¹□□Lu-DOTATATE: the IEO phase I-II study. Eur J Nucl Med Mol Imaging. 2011;38(12):2125–35. https://doi.org/10.1007/s00259-011-1902-1

7. Bodei L, Kidd M, Paganelli G, Grana CM, Drozdov I, Cremonesi M, et al. Long-term tolerability of PRRT in 807 patients with neuroendocrine tumours: the value and limitations of clinical factors. Eur J Nucl Med Mol Imaging. 2015;42(1):5–19. https://doi.org/10.1007/s00259-014-2893-5

8. Kam BL, Teunissen JJ, Krenning EP, de Herder WW, Khan S, van Vliet EI, et al. Lutetium-labelled peptides for therapy of neuroendocrine tumours. Eur J Nucl Med Mol Imaging. 2012;39(Suppl 1):S103–12. https://doi.org/10.1007/s00259-011-2039-y

9. Van Vliet EI, Teunissen JJ, Kam BL, de Jong M, Krenning EP, Kwekkeboom DJ. Treatment of gastroenteropancreatic neuroendocrine tumors with peptide receptor radionuclide therapy. Neuroendocrinology. 2013;97(1):74–85. https://doi.org/10.1159/000335018

10. Oyen WJ, Bodei L, Giammarile F, Maecke HR, Tennvall J, Luster M, et al. Targeted therapy in nuclear medicine–current status and future prospects. Ann Oncol. 2007;18(11):1782-1792. https://doi.org/10.1093/annonc/mdm111

11. Ilan E, Sandström M, Wassberg C, Sundin A, Garske-Román U, Eriksson B, et al. Dose response of pancreatic neuroendocrine tumors treated with peptide receptor radionuclide therapy using ^{177}Lu-DOTATATE. J Nucl Med. 2015;56(2):177–82. https://doi.org/10.2967/jnumed.114.148437

12. Kwekkeboom DJ, Bakker WH, Kooij PP, et al. [^{177}Lu-DOTAOTyr3]octreotate: comparison with [^{111}In-DTPAo]octreotide in patients. Eur J Nucl Med. 2001;28(9):1319–25. https://doi.org/10.1007/s002590100574

13. Sandström M, Garske-Román U, Granberg D, Johansson S, Widström C, Eriksson B, et al. Individualized dosimetry of kidney and bone marrow in patients undergoing ^{177}Lu-DOTA-octreotate treatment. J Nucl Med. 2013;54(1):33–41. https://doi.org/10.2967/jnumed.112.107524

14. Bailey DL, Hennessy TM, Willowson KP, Henry EC, Chan DL, Aslani A, et al. In vivo quantification of ^{177}Lu with planar whole-body and SPECT/CT gamma camera imaging. EJNMMI Phys. 2015;2(1):20. https://doi.org/10.1186/s40658-015-0123-2

15. Hippeläinen E, Tenhunen M, Mäenpää H, Sohlberg A. Quantitative accuracy of ^{177}Lu SPECT reconstruction using different compensation methods: phantom and patient studies. EJNMMI Res. 2016;6(1):16. https://doi.org/10.1186/s13550-016-0172-0

16. Ljungberg M, Celler A, Konijnenberg MW, Eckerman KF, Dewaraja YK, Sjögreen-Gleisner K, et al. MIRD Pamphlet No. 26: Joint EANM/MIRD Guidelines for Quantitative ^{177}Lu SPECT applied for dosimetry

of radiopharmaceutical therapy. J Nucl Med. 2016;57(1):151–62. https://doi.org/10.2967/jnumed.115.159012

17. Ljungberg M, Sjögreen Gleisner K. Personalized dosimetry for radionuclide therapy using molecular imaging tools. Biomedicines. 2016;4(4):25. https://doi.org/10.3390/biomedicines4040025

18. Frey EC, Humm JL, Ljungberg M. Accuracy and precision of radioactivity quantification in nuclear medicine images. Semin Nucl Med. 2012;42(3):208–18. https://doi.org/10.1053/j.semnuclmed.2011.11.003

19. Garkavij M, Nickel M, Sjögreen-Gleisner K, Ljungberg M, Ohlsson T, Wingårdh K, et al. ^{177}Lu-[DOTA0,Tyr3] octreotate therapy in patients with disseminated neuroendocrine tumors: Analysis of dosimetry with impact on future therapeutic strategy. Cancer. 2010;116(4 Suppl):1084–92. https://doi.org/10.1002/cncr.24796

20. Guerriero F, Ferrari ME, Botta F, Fioroni F, Grassi E, Versari A, et al. Kidney dosimetry in ¹⁷⁷Lu and ⁹⁰Y peptide receptor radionuclide therapy: influence of image timing, time-activity integration method, and risk factors. Biomed Res Int. 2013;2013:935351. https://doi.org/10.1155/2013/935351

21. Hudson HM, Larkin RS. Accelerated image reconstruction using ordered subsets of projection data. IEEE Trans Med Imaging. 1994;13(4):601–9. https://doi.org/10.1109/42.363108

22. Alzimami KS, Sassi SA, Spyrou NM. A comparison between 3D OSEM and FBP image reconstruction algorithms in SPECT. In: Ao SI, Gelman L, editors. Advances in electrical engineering and computational science. Lecture Notes in Electrical Engineering, vol 39. Dordrecht: Springer; 2009. pp 195–206. https://doi.org/10.1007/978-90-481-2311-7_17

23. Sowa-Staszczak A, Lenda-Tracz W, Tomaszuk M, Głowa B, Hubalewska-Dydejczyk A. Optimization of image reconstruction method for SPECT studies performed using [⁹⁹^{m}Tc-EDDA/HYNIC] octreotate in patients with neuroendocrine tumors. Nucl Med Rev Cent East Eur. 2013;16(1):9–16. https://doi.org/10.5603/NMR.2013.0003

24. Yokoi T, Shinohara H, Onishi H. Performance evaluation of OSEM reconstruction algorithm incorporating three-dimensional distance-dependent resolution compensation for brain SPECT: a simulation study. Ann Nucl Med. 2002;16(1):11–8. https://doi.org/10.1007/BF02995286

25. Kemin H. Impact of different reconstruction algorithms and OSEM reconstruction parameters on quantitative results in SPECT/CT. J Nucl Med. 2018;59(Suppl 1):1800.

26. Dewaraja YK, Frey EC, Sgouros G, Brill AB, Roberson P, Zanzonico PB, et al. MIRD pamphlet No. 23: quantitative SPECT for patient-specific 3-dimensional dosimetry in internal radionuclide therapy. J Nucl Med. 2012;53(8):1310–25. https://doi.org/10.2967/jnumed.111.100123

27. Dewaraja YK, Wilderman SJ, Ljungberg M, Koral KF, Zasadny K, Kaminiski MS. Accurate dosimetry in ^{131}I radionuclide therapy using patient-specific, 3-dimensional methods for SPECT reconstruction and absorbed dose calculation. J Nucl Med. 2005;46(5):840–9.

28. Frey EC, Tsui BM. A new method for modeling the spatially-variant, object-dependent scatter response function in SPECT. 1996 IEEE Nuclear Science Symposium. Conference Record, Anaheim, CA, USA; 1996, pp. 1082-1086 vol. 2. https://doi.org/10.1109/NSSMIC.1996.591559

29. Tran-Gia J, Lassmann M. Optimizing image quantification for ^{177}Lu SPECT/CT based on a 3D printed 2-compartment kidney phantom. J Nucl Med. 2018;59(4):616–24. https://doi.org/10.2967/jnumed.117.200170

30. He B, Frey EC. The impact of 3D volume of interest definition on accuracy and precision of activity estimation in quantitative SPECT and planar processing methods. Phys Med Biol. 2010;55(12):3535–44. https://doi.org/10.1088/0031-9155/55/12/017

31. International Atomic Energy Agency. Quantitative SPECT OR SPECT/CT imaging. In:

Quantitative nuclear medicine imaging: Concepts, requirements and methods. IAEA Human Health Report No.9. IAEA, Vienna, Austria; 2014. pp. 27–36.

32. Erlandsson K, Thomas B, Dickson J, Hutton BF. Partial volume correction in SPECT reconstruction with OSEM. Nucl Instrum Meth A. 2011;648(Suppl 1):S85–8. https://doi.org//10.1016/j.nima.2010.12.106

33. Willowson K, Bailey DL, Baldock C. Quantitative SPECT reconstruction using CT-derived corrections. Phys Med Biol. 2008;53(12):3099–112. https://doi.org/10.1088/0031-9155/53/12/002

34. Adams MC, Turkington TG, Wilson JM, Wong TZ. A systematic review of the factors affecting accuracy of SUV measurements [published correction appears in AJR Am J Roentgenol. 2010 Oct;195(4):1043]. AJR Am J Roentgenol. 2010;195(2):310–20. https://doi.org/10.2214/AJR.10.4923

35. de Wit TC, Xiao J, Nijsen JF, van het Schip FD, Staelens SG, van Rijk PP, et al. Hybrid scatter correction applied to quantitative holmium-166 SPECT. Phys Med Biol. 2006;51(19):4773–87. https://doi.org/10.1088/0031-9155/51/19/004

36. He B, Du Y, Song X, Segars WP, Frey EC. A Monte Carlo and physical phantom evaluation of quantitative In-111 SPECT. Phys Med Biol. 2005;50(17):4169–85. https://doi.org/10.1088/0031-9155/50/17/018

37. National Electrical Manufacturers Association. NEMA NU 1: 2012. Performance measurements of gamma cameras. Rosslyn, Virginia: National Electrical Manufacturers Association; 2012.

38. Shcherbinin S, Celler A, Belhocine T, Vanderwerf R, Driedger A. Accuracy of quantitative reconstructions in SPECT/CT imaging. Phys Med Biol. 2008;53(17):4595–4604. https://doi.org/10.1088/0031-9155/53/17/009

39. D'Arienzo M, Cazzato M, Cozzella ML, Cox M, D'Andrea M, Fazio A, et al. Gamma camera calibration and validation for quantitative SPECT imaging with ^{177}Lu. Appl Radiat Isot. 2016;112:156–64. https://doi.org/10.1016/j.apradiso.2016.03.007

40. Zhao W, Esquinas PL, Hou X, Uribe CF, Gonzalez M, Beauregard J-M, et al. Determination of gamma camera calibration factors for quantitation of therapeutic radioisotopes. EJNMMI Phys. 2018;5(1):8. https://doi.org/10.1186/s40658-018-0208-9

41. Ljungberg M, Strand SE. A Monte Carlo program for the simulation of scintillation camera characteristics. Comput Methods Programs Biomed. 1989;29(4):257–72. https://doi.org/10.1016/0169-2607(89)90111-9

42. Wevrett J, Fenwick A, Scuffham J, Nisbet A. Development of a calibration protocol for quantitative imaging for molecular radiotherapy dosimetry. Radiat Phys Chem. 2017;140:355–60. https://doi.org/10.1016/j.radphyschem.2017.02.053

43. Wevrett J, Fenwick A, Scuffham J, Johansson L, Gear J, Schlögl S, et al. Inter-comparison of quantitative imaging of lutetium-177 (^{177}Lu) in European hospitals. EJNMMI Phys. 2018;5(1):17. https://doi.org/10.1186/s40658-018-0213-z

44. Ramonaheng K, van Staden JA, du Raan H. Validation of a Monte Carlo modelled gamma camera for Lutetium-177 imaging. Appl Radiat Isot. 2020;163:109200. https://doi.org/10.1016/j.apradiso.2020.109200

45. Yushkevich PA, Piven J, Hazlett HC, Smith RG, Ho S, Gee JC, et al. User-guided 3D active contour segmentation of anatomical structures: significantly improved efficiency and reliability. Neuroimage. 2006;31(3):1116–28. https://doi.org/10.1016/j.neuroimage.2006.01.015

46. Beauregard JM, Hofman MS, Pereira JM, Eu P, Hicks RJ. Quantitative ^{177}Lu SPECT (QSPECT) imaging using a commercially available SPECT/CT system. Cancer Imaging. 2011;11(1):56–66. https://doi.org/10.1102/1470-7330.2011.0012

47. He B, Nikolopoulou A, Osborne J, Vallabhajosula S, Goldsmith S. Quantitative SPECT imaging with Lu-177: A physical phantom evaluation. J Nucl Med. 2012;53(Suppl 1):2407.

48. Shcherbinin S, Piwowarska-Bilska H, Celler A, Birkenfeld B. Quantitative SPECT/CT reconstruction for ¹⁷⁷Lu and ¹⁷⁷Lu/⁹⁰Y targeted radionuclide therapies. Phys Med Biol. 2012;57(18):5733–47. https://doi.org/10.1088/0031-9155/57/18/5733

49. Brolin G, Gustafsson J, Ljungberg M, Gleisner KS. Pharmacokinetic digital phantoms for accuracy assessment of image-based dosimetry in ^{177}Lu-DOTATATE peptide receptor radionuclide therapy. Phys Med Biol. 2015;60(15):6131–49. https://doi.org/10.1088/0031-9155/60/15/6131

50. Frey EC, Tsui BM. A practical method for incorporating scatter in a projector-backprojector for accurate scatter compensation in SPECT. IEEE Trans Nucl Sci 1993;40(4):1107–16. https://doi.org/10.1109/23.256720

51. Loening AM, Gambhir SS. AMIDE: a free software tool for multimodality medical image analysis. Mol Imaging. 2003;2(3):131–7. https://doi.org/10.1162/153535003322556877

52. Robinson AP, Tipping J, Cullen DM, Hamilton D, Brown R, Flynn A, et al. Organ-specific SPECT activity calibration using 3D printed phantoms for molecular radiotherapy dosimetry. EJNMMI Phys. 2016;3(1):12. https://doi.org/10.1186/s40658-016-0148-1

53. Willowson KP, Eslick E, Ryu H, Poon A, Bernard EJ, Bailey DL. Feasibility and accuracy of single time point imaging for renal dosimetry following ^{177}Lu-DOTATATE ('Lutate') therapy. EJNMMI Phys. 2018;5(1):33. https://doi.org/10.1186/s40658-018-0232-9

54. Uribe CF, Esquinas PL, Tanguay J, Gonzalez M, Gaudin E, Beauregard J-M, et al. Accuracy of ^{177}Lu activity quantification in SPECT imaging: a phantom study. EJNMMI Phys. 2017;4(1):2. https://doi.org/10.1186/s40658-016-0170-3

55. de Nijs R, Lagerburg V, Klausen TL, Holm S. Improving quantitative dosimetry in ^{177}Lu-DOTATATE SPECT by energy window-based scatter corrections. Nucl Med Commun. 2014;35(5):522–33. https://doi.org/10.1097/MNM.0000000000000079

56. Mezzenga E, D'Errico V, D'Arienzo M, Strigari L, Panagiota K, Matteucci F, et al. Quantitative accuracy of ^{177}Lu SPECT imaging for molecular radiotherapy. PLoS One. 2017;12(8):e0182888. https://doi.org/10.1371/journal.pone.0182888

57. Dewaraja YK, Ljungberg M, Green AJ, Zanzonico PB, Frey EC, SNMMI MIRD Committee, et al. MIRD pamphlet No. 24: Guidelines for quantitative ^{131}I SPECT in dosimetry applications. J Nucl Med. 2013;54(12):2182–8. https://doi.org/10.2967/jnumed.113.122390

58. Dewaraja YK, Koral KF, Fessler JA. Regularized reconstruction in quantitative SPECT using CT side information from hybrid imaging. Phys Med Biol. 2010;55(9):2523–39. https://doi.org/10.1088/0031-9155/55/9/007

59. Tsui BM, Frey EC, Zhao X, Lalush DS, Johnston RE, McCartney WH. The importance and implementation of accurate 3D compensation methods for quantitative SPECT. Phys Med Biol. 1994;39(3):509–30. https://doi.org/10.1088/0031-9155/39/3/015

60. Sanders JC, Kuwert T, Hornegger J, Ritt P. Quantitative SPECT/CT imaging of ^{177}Lu with in vivo validation in patients undergoing peptide receptor radionuclide therapy. Mol Imaging Biol. 2014;17(4):585–93. https://doi.org/10.1007/s11307-014-0806-4

61. Tran-Gia J, Lassmann M. Characterization of noise and resolution for quantitative ^{177}Lu SPECT/CT with xSPECT Quant. J Nucl Med. 2019;60(1):50–9. https://doi.org/10.2967/jnumed.118.211094

62. Peters SM, Meyer Viol SL, van der Werf NR, de Jong N, van Velden FH, Meeuwis A, et al. Variability in lutetium-177 SPECT quantification between different state-of-the-art SPECT/CT systems. EJNMMI Phys. 2020;7(1):9. https://doi.org/10.1186/s40658-020-0278-3

63. D'Arienzo M, Cozzella ML, Fazio A, De Felice P, Iaccarino G, D'Andrea M, et al. Quantitative ^{177}Lu SPECT imaging using advanced correction algorithms in non-reference geometry. Phys Med. 2016;32(12):1745–52. https://doi.org/10.1016/j.ejmp.2016.09.014

64. International Commission on Radiation Units and Measurements. ICRU Report 67: Absorbed-dose specification in nuclear medicine. J ICRU. 2002;2(1):3–110.

Figures

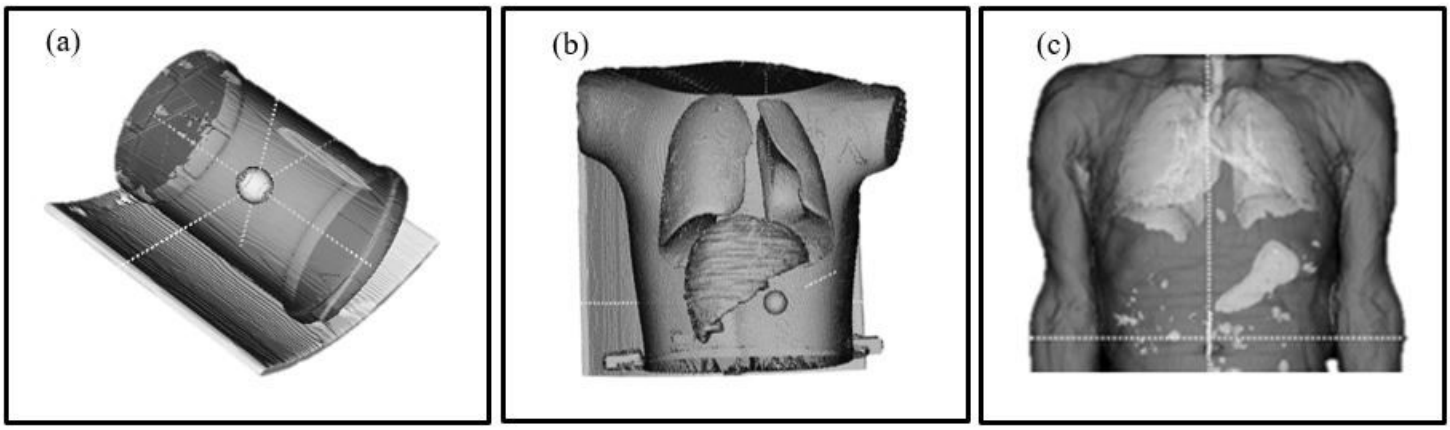

Figure 1

Segmented images of the (a) cylindrical (b) torso and (b) patient phantoms

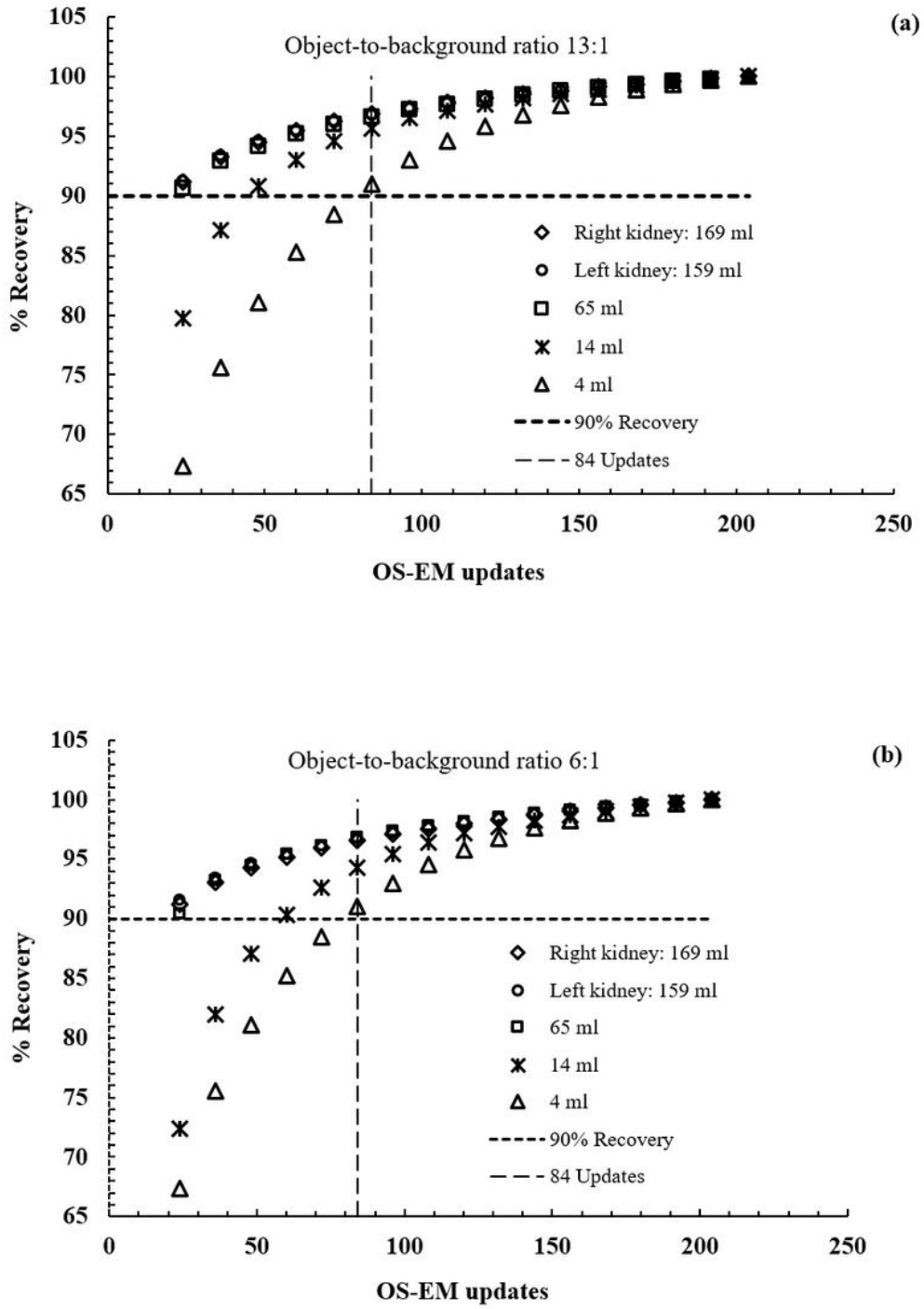

Figure 2

Counts recovered (%) from reconstructed images as a function of 3D OS-EM updates for different size spheres simulated inside a cylindrical phantom as well as for the right and left kidney of a patient phantom with object-to-background ratios of (a) 13:1 and (b) 6:1. Reconstruction included CT-based attenuation correction, effective source scatter estimation (ESSE) scatter correction and collimator detector response (CDR) compensation

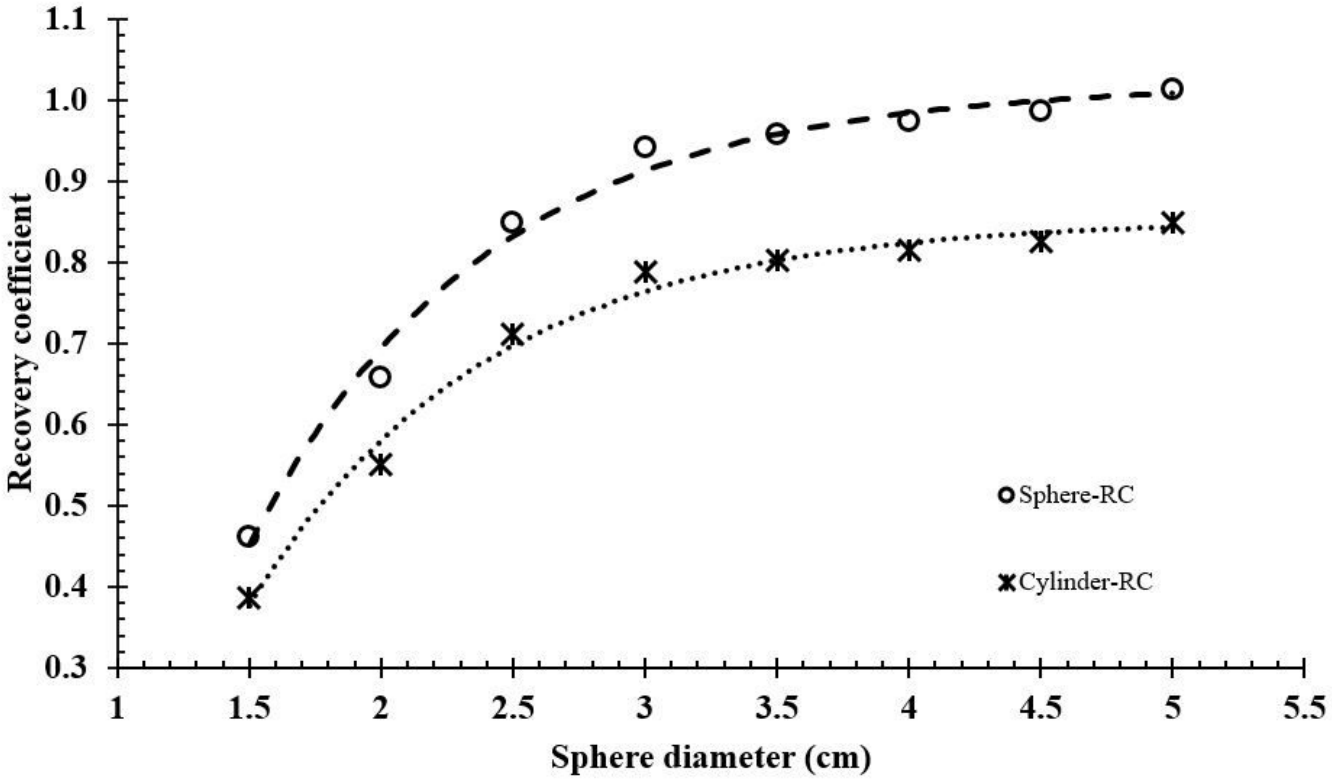

Figure 3

Recovery coefficient (RC) curves generated using a sphere calibration factor (CF) and a cylinder calibration factor (CF) plotted for different sphere sizes

Figure 4

Reconstructed coronal slices of the patient phantom illustrating the (a) sphere and (b) kidneys used to determine the quantification error